sustainability

MDPI

Article

Dynamic Visibility Recognition and Driving Risk Assessment Under Rain–Fog Conditions Using Monocular Surveillance Imagery

Zilong Xie [1], Chi Zhang [1,*], Dibin Wei [1], Xiaomin Yan [1] and Yijing Zhao [2]

[1] School of Highway, Chang'an University, Xi'an 710064, China; 2022021075@chd.edu.cn (Z.X.); 2023121166@chd.edu.cn (D.W.); yanxm@chd.edu.cn (X.Y.)
[2] College of Transportation Engineering, Chang'an University, Xi'an 710064, China; zhaoyj9931@163.com
* Correspondence: zhangchi@chd.edu.cn

Abstract

This study addresses the limitations of conventional highway visibility monitoring under rain–fog conditions, where fixed stations and visibility sensors provide limited spatial coverage and unstable accuracy. Considering that drivers' visual fields are jointly affected by global fog and local spray-induced mist, a dynamic visibility recognition and risk assessment framework is proposed using roadside monocular CCTV (Closed-Circuit Television) imagery. The method integrates the Koschmieder scattering model with the dark channel prior to estimate atmospheric transmittance and derives visibility through lane-line calibration. A Monte Carlo-based coupling model simulates local visibility degradation caused by tire spray, while a safety potential field defines the low-visibility risk field force (LVRFF) combining dynamic visibility, relative speed, and collision distance. Results show that this approach achieves over 86% accuracy under heavy rain, effectively captures real-time visibility variations, and that LVRFF exhibits strong sensitivity to visibility degradation, outperforming traditional safety indicators in identifying high-risk zones. By enabling scalable, infrastructure-based visibility monitoring without additional sensing devices, the proposed framework reduces deployment cost and energy consumption while enhancing the long-term operational resilience of highway systems under adverse weather. From a sustainability perspective, the method supports safer, more reliable, and resource-efficient traffic management, contributing to the development of intelligent and sustainable transportation infrastructure.

Keywords: visibility; water spray; fog; CCTV; expressway; driving risk; sustainable transportation; intelligent highway

Academic Editor: Virginia P. Sisiopiku

Received: 30 October 2025
Revised: 20 December 2025
Accepted: 5 January 2026
Published: 7 January 2026

1. Introduction

The frequency and intensity of extreme weather and climate events in China have been increasing, with the climate risk index showing a rising trend. Among these, the impacts of rainy and foggy weather on driving safety have become increasingly severe [1]. Among these, visibility, as the most direct visual perception parameter, has a decisive impact on driver decision-making behavior [2]. In the central and eastern regions of China—particularly along the Yangtze River and in the hilly areas of Jiangnan—unique climatic and geographical conditions have led to the formation of prominent fog-prone

zones [3]. In some areas, annual rainfall commonly exceeds 1200 mm, and composite meteorological phenomena such as overlapping rainfall and fog frequently occur in autumn and winter, further exacerbating visibility deterioration.

Existing studies have shown that rainfall affects driving safety through two primary mechanisms: on the one hand, it reduces road surface friction, thereby compromising braking performance [4,5]; on the other hand, tire–pavement interactions under wet conditions generate water spray, which acts as an aerosol and instantly diminishes the visibility of following vehicles [6]. Although the frictional effect of rainfall has been extensively investigated, the impact of water spray has often been overlooked in highway safety research. In reality, fog and water spray exhibit significant optical and dynamic coupling characteristics. Fog consists mainly of fine droplets (1–10 μm) that cause Mie scattering of visible light, leading to reduced transmittance and blurred perception of distant objects, whereas spray droplets (20–200 μm) create stronger localized occlusion effects. When vehicles travel at high speeds, tire-induced spray becomes entrained and dispersed within the wake flow, interacting with ambient fog droplets to produce multiple and composite scattering events. This interaction substantially intensifies local light attenuation, forming a non-uniform visibility field characterized by steep spatial gradients and rapid temporal fluctuations. Particularly under conditions of heavy rainfall or low wind speed, prolonged spray residence time amplifies its coupling with background fog, resulting in transient but severe degradation of local visibility. Therefore, achieving real-time, spatially resolved visibility monitoring to support driver warning and roadway management has become a crucial challenge for ensuring expressway safety in fog-prone regions.

It can thus be concluded that the reduction in driver visibility can be classified into two conditions: one is global visibility degradation caused by natural fog when no leading vehicle is present; the other is localized visibility reduction induced by water spray generated from a preceding vehicle on a wet pavement. The driving risk arising from the coupling of global and local visibility is clearly subject to rapid real-time variations with changes in water film thickness, vehicle speed, following distance, and fog density.

Significant progress has been made in recent years in machine vision-based detection methods for addressing global visibility degradation caused by fine aerosol droplets suspended in the air. With the rapid expansion of highway surveillance systems, vision-based monitoring has gradually replaced traditional physical visibility sensors. For instance, Zhang et al. proposed a real-time visibility detection framework using densely distributed roadside cameras [7], demonstrating the feasibility of large-scale visual meteorological monitoring. Deep learning methods have further advanced this field. Xiao et al. developed a deep neural network architecture that fuses spectral and depth features extracted from highway surveillance imagery, achieving higher precision and recall than conventional visibility meters [8]. Li et al. introduced an attention-based BiLSTM-CNN network for visibility prediction, where the attention mechanism effectively captured spatiotemporal variations in visual degradation [9]. Despite their promising performance, neural network models still face practical limitations regarding computational efficiency and hardware cost for deployment in engineering environments.

Consequently, traditional computer vision methods remain of considerable value for low-cost, scalable visibility monitoring. Sun et al. proposed a vision-geometry-driven visibility prediction framework that leverages lane-related features to enhance estimation accuracy [10]. He et al. applied the dark channel prior algorithm for image defogging from lane-line coordinates, thereby eliminating the need for camera calibration [11]. Guo et al. further introduced a differential regression network that adapts to visual similarity variations across different weather and seasonal conditions, significantly improving prediction robustness [2]. Overall, surveillance imagery now provides richer and more reliable input data, while traditional vision-based techniques continue to offer advantages in

terms of simplicity, cost-effectiveness, and real-time feasibility—forming a complementary path alongside deep learning approaches toward practical, engineering-grade visibility estimation.

The reduction in rearward visibility caused by water spray generated from tire–water film interaction can be regarded as a form of localized visibility degradation. This complex process is currently investigated primarily through modeling and experimental studies. There has also been research into the spray and splash generated by tires on wet roads. On the simulation front, Flintsch et al. used SPH (Smoothed Particle Hydrodynamics) methods to study spray characteristics from airplane tires on flooded runways, identifying four spray types and their formation mechanisms [6]. Qu simulated the effects of tire speed and water film thickness on spray using SPH (Smoothed Particle Hydrodynamics), providing insight for engine water ingestion risk assessment [12]. Wang et al. applied a Monte Carlo model to simulate photon scattering in water mist aerosols and proposed a visibility model using water film thickness and vehicle speed as variables [13]. On the experimental side, the Society of Automotive Engineers (SAE) has issued official guidelines for evaluating spray clouds via optical extinction and contrast [14]. Do, M.T. et al. established a nonlinear relationship between tire spray and pavement texture depth through experiments [15]. Whether on aircraft runways or wet highways, tire-induced spray affects visibility to varying degrees depending on water film thickness, vehicle speed, vehicle type, and pavement structure. Developing a real-time, dynamic visibility model remains a major challenge for digital road infrastructure under adverse weather conditions.

In summary, the main monitoring difficulty faced by highway systems lies in the significant spatial variability of meteorological parameters due to the spatial extensiveness of linear infrastructure (often spanning tens to hundreds of kilometers). The dynamically coupled visibility field varies greatly (affected by vehicle speed and water film thickness during spray formation). Existing fixed-point meteorological sensors (e.g., visibility meters) are constrained by their location and sampling frequency, making it difficult to capture visibility changes around moving vehicles. This study thus focuses on two key scientific questions: (1) how to develop a dynamic image-based visibility recognition method capable of identifying atmospheric visibility and water spray phenomena; (2) how to build a visibility calculation model that couples mechanical spray and natural fog. Solving these problems holds great practical significance for the development of intelligent real-time warning systems and the optimization of road segment management strategies.

Here we couple monocular surveillance imagery with a Monte Carlo-based multiple-scattering model to retrieve pixel-level visibility. Specifically:

(i) The Materials and Methods establishes a visibility estimation model based on the dark channel prior theory, integrating lane line geometric calibration to compute image transmittance for global visibility estimation. Through optical experiments on tire splash aerosol and Monte Carlo scattering simulations, a dynamic coupling model for local visibility loss is developed. Building on localized visibility impairment, a safety potential field model is introduced that incorporates dynamic visibility, inter-vehicle distance, and relative speed to construct a real-time quantifiable driving risk indicator LVRFF (low-visibility risk field force).

(ii) In the Results, we summarize the preprocessing of vehicle trajectory tracking from surveillance data and road pixel coordinate transformation, with detailed explanation of the dynamic visibility model construction.

(iii) The discussion section presents comparative analysis between visibility calculations using the dark channel prior algorithm versus meteorological station data and laser sensor measurements, demonstrating the method's accuracy and robustness. Further

comparisons highlight the advantages of the LVRFF over traditional conflict indicators.

2. Materials and Methods

The overall technical route of this study is shown in Figure 1.

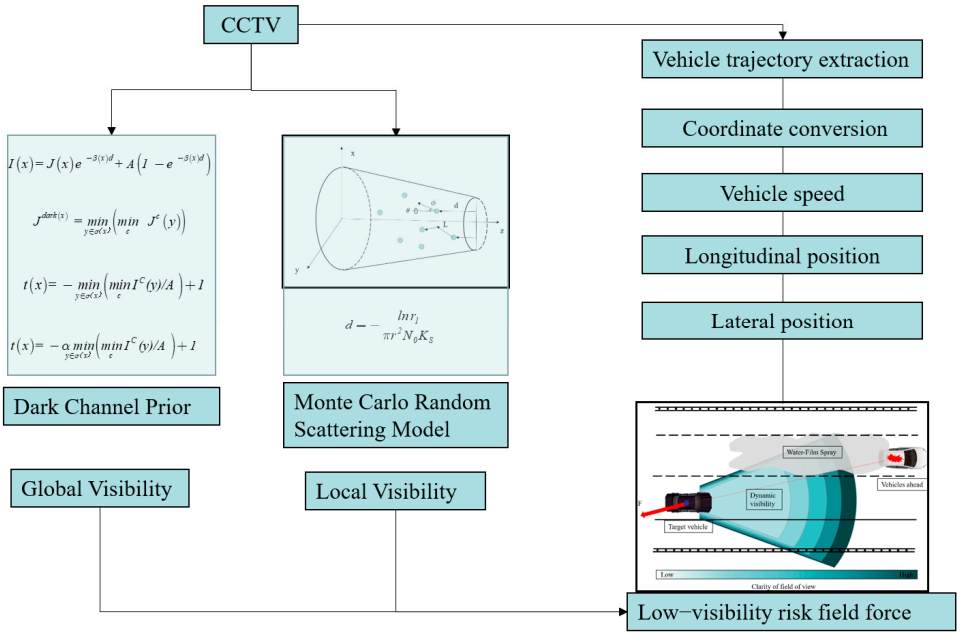

Figure 1. Dynamic Visibility Detection and Vehicle Risk Quantification on Highways.

2.1. Vehicle Trajectory Information Extraction and Coordinate Conversion

Relying on the roadside CCTV video data collected by CY Expressway in Sichuan Province, China, the camera is located at stake k176+372, from 7:00 to 10:18 on 4 November 2022, with a duration of about 3 h. The weather is light rain to clear, there is fog interfering with visibility in the road section, and there is a certain thickness of water film on the ground, which gradually dries over time. During the data collection period, the total number of vehicles passing through the road section: 537, small vehicles: 395, large vehicles: 142. The focal length of the camera is 6.2 mm, the height above the ground is 6.5 m, and the layout position is in the center of the separation belt.

In order to realize the vehicle detection and recognition, the research selects the Yolo V5 deep learning algorithm model, which uses a single neural network to predict the rectangular boundary and category probability of each object in a single forward transfer, and has the advantages of fast detection speed and convenient deployment. At the same time, in order to realize the continuous tracking of vehicle trajectory, the research selects the stone sort algorithm to realize the continuous tracking of vehicle trajectory. The algorithm predicts the continuous position of the detection target based on the Siamese network and Kalman filter. This tracking algorithm is also more suitable for developing road monitoring data with lower deployment cost and complexity.

To accurately extract vehicle motion information and calculate the extinction coefficient using the dark channel prior algorithm, this study adopts a monocular vision-based camera calibration method. The internal and external parameters of the camera—including rotation angle, pitch angle, focal length, and installation height—are computed, and a coordinate transformation is achieved by establishing a mapping between the image coordinate system and the world coordinate system [16]. The “VWL” method is employed

for camera calibration [17], which determines the camera parameters based on fixed road marking lengths and spacing. Once the camera parameters are obtained, a conversion between the three-dimensional physical coordinate system and the image pixel coordinates is performed according to Equation (1). The camera focal length is 8.35 mm, the camera rotation angle is −0.0649 rad, the camera pitch angle is 0.2418 rad, and the camera height is 6.50 m. The process of coordinate transformation and camera calibration is illustrated in Figure 2.

$$\begin{bmatrix} \alpha u \\ \alpha v \\ \alpha \end{bmatrix} = \begin{bmatrix} f\cos\theta & -f\sin\theta & 0 & 0 \\ -f\sin\phi\sin\theta & -f\sin\phi\cos\theta & -f\cos\phi & fh\cos\phi \\ \cos\phi\sin\theta & \cos\phi\cos\theta & -\sin\phi & h\sin\phi \end{bmatrix} \begin{bmatrix} x \\ y \\ z \\ 1 \end{bmatrix} \quad (1)$$

where f : camera focal length; θ: camera rotation angle; ϕ: camera pitch angle; h: camera height (all classified as external camera parameters); α: scale factor; (u, v) : coordinates of a point in the image coordinate system; and (x, y, z) : corresponding coordinates in the real-world 3D coordinate system.

As shown in Figure 2, a vanishing point is determined based on the road markings, as illustrated in Figure 2b. A set of parallel road markings is selected as the width calibration reference, and a road marking with a known length is chosen as the length calibration reference, as shown in Figure 2a. Considering the accuracy requirements for monitoring vehicle motion information, an effective monitoring area is selected based on the real-world distance corresponding to each pixel. The coordinate projection of this area is shown in Figure 2c. The effective monitoring area has a width of 11.34 m and a length of 69 m.

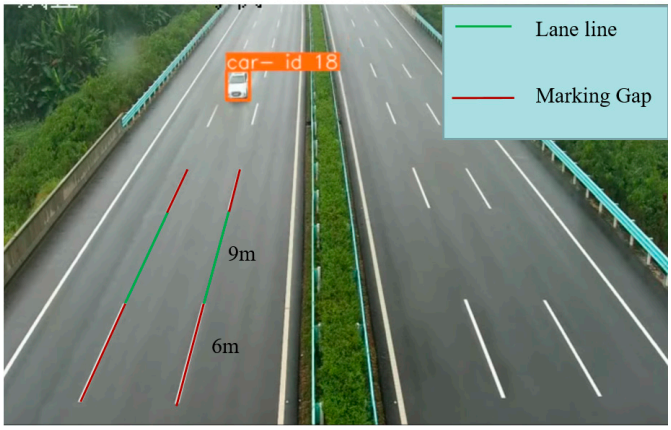

(**a**) Road marking reference

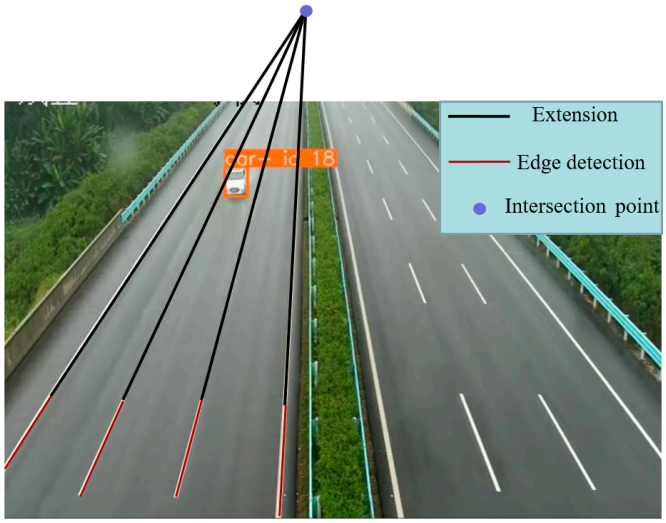

(**b**) Extension line intersection detection

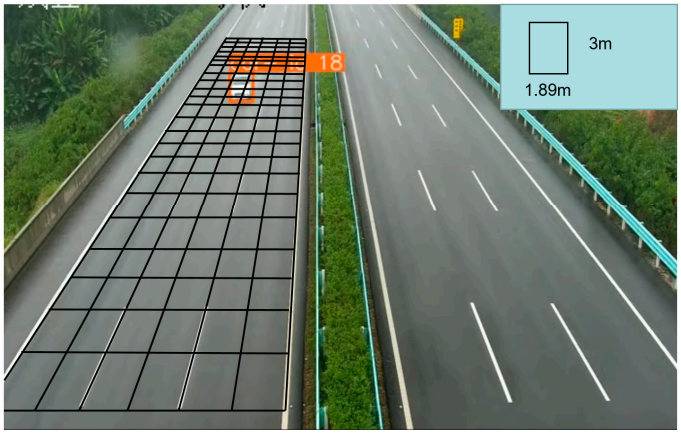

(**c**) Road grid projection

Figure 2. Camera calibration and coordinate system projection.

2.2. Image-Based Visibility Estimation Using the Dark Channel Prior Algorithm

This study directly computes visibility by estimating atmospheric transmittance from surveillance images, and this machine vision-based approach is enabled by the dark channel prior theory. Atmospheric transmittance describes the proportion of light that reaches the camera after passing through fog and suspended droplets, and its decay is governed by the extinction coefficient, which quantifies the attenuation of light per unit distance. Higher extinction coefficients correspond to stronger scattering, reduced visual contrast, and shorter visibility distances. The dark channel prior provides an effective means to infer transmittance from a single image by exploiting the observation that, under normal outdoor conditions, at least one color channel in non-sky regions contains very low pixel intensities. In foggy weather, these normally dark pixels become brighter due to airlight, and the degree of deviation from their expected minima allows transmittance—and subsequently the extinction coefficient—to be estimated. By integrating the dark channel prior with the physical atmospheric scattering model, the method establishes a mapping from pixel-level optical characteristics to real-world meteorological visibility, enabling robust visibility estimation without relying on specialized instruments.

Under low-visibility weather conditions such as fog and haze, visibility estimation based on scattering theory requires the calculation of atmospheric transmittance and extinction coefficient. To address this challenge, this study integrates a physical model of atmospheric scattering with the dark channel prior theory and proposes a method for estimating visibility using a single image frame. First, based on Koschmieder's law [18], an

atmospheric scattering model is established to reveal the quantitative relationship between the brightness attenuation of a target object, transmittance, and extinction coefficient. Then, leveraging the dark channel prior theory [11]—originally developed for image defogging—a transmittance estimation model is constructed by analyzing the minimum channel characteristics of non-sky region pixels. Considering the refractive effects of aerosol particles in the actual atmosphere, an empirical correction factor is introduced to adjust the estimated transmittance. Finally, by establishing a conversion relationship between transmittance and the extinction coefficient, the model enables the mapping from image features to meteorological visibility parameters. This method reduces the reliance on specialized instruments in traditional visibility observation and provides a robust theoretical framework for vision-based visibility monitoring. As light propagates through foggy conditions, it interacts with suspended particles in the atmosphere, resulting in scattering effects including attenuation and airlight. Based on the phenomenon of light scattering, the image of a target object $I(x)$ captured by CCTV equipment can be expressed by Equation (2).

$$I(x) = J(x)e^{-\beta(x)d} + A\left(1 - e^{-\beta(x)d}\right) \tag{2}$$

Here x: the wavelength of light, $J(x)$: the intrinsic brightness of the object, A: the global atmospheric light value, β: the extinction coefficient, and d: the optical distance between the monitoring device and the observed object.

Based on Koschmieder's law and the attenuation principle of atmospheric light propagation, image contrast decreases exponentially with increasing distance. The contrast C can be expressed by Equation (3).

$$C = C_0 e^{-\beta d} \tag{3}$$

Here C: the brightness contrast value received by the sensing device at an optical distance d; and C_0: the relative brightness difference between the object and its surrounding environment.

According to research definitions, visibility refers to the maximum horizontal distance at which a person with normal vision can clearly see and identify the outline of an object against the sky background under specific weather conditions [19], or recognize a luminous point at night. As defined by authoritative meteorological organizations [20], when the contrast between the target and its background drops to a certain threshold value, the maximum distance at which the human eye can observe the target is termed the meteorological visibility distance. Therefore, the visibility V can be expressed by Equation (4):

$$V = \frac{-ln(0.05)}{\beta} \tag{4}$$

According to Equation (3), if the target formula calculates visibility according to the monitoring image, the extinction coefficient can be observed as an alternative index.

He et al. proposed that in most non-sky regions of an outdoor image, some pixels always have the smallest pixel value in the R, G, B three color channel (at least one color channel), and the minimum value of light intensity in this area is very small (tending to 0) [11]. According to its definition, the expression of dark channel image is Equation (5):

$$J^{dark(x)} = \min_{y \in \sigma(x)} \left(\min_{c} J^{c}(y) \right) \tag{5}$$

where $J^{dark(x)}$: the dark channel image of the image; $J^{c}(y)$: a color channel of J; c: the index value of RGB three primary color channel; $\min_{y\in\sigma(x)}$: the minimum value in the neighborhood of pixel X; $\min_{c}$: a pixel of a color channel in the image is minimized. And based on the dark channel prior theory, the study found that the dark channel value of other regions except the sky region always tended to 0.

According to the light scattering theoretical model mentioned above, it is combined with the dark channel prior theory. When solving the atmospheric transmittance value, it is necessary to first calculate the global atmospheric light value A, conduct dark channel treatment for Equation (1), and take the minimum value in the local windows on both sides and R, G, B channels. I^{C} represents the input hazy image, which is first normalized by the global atmospheric light value A, and then processed using the definition of the dark channel to obtain its dark channel map. The atmospheric transmittance can be obtained as follows Equation (6):

$$t(x) = -\min_{y\in\sigma(x)}\left(\min_{c} I^{C}(y)/A\right) + 1 \tag{6}$$

Since the atmosphere itself contains fine dust, water vapor and other components, which will have refractive effects on the image reading of the sensor and human eyes, the atmospheric transmittance is reduced as Equation (7), α is the haze-preserving coefficient, typically set to 0.95 [21]:

$$t(x) = -\alpha\min_{y\in\sigma(x)}\left(\min_{c} I^{C}(y)/A\right) + 1 \tag{7}$$

2.3. Visibility Estimation Model for Tire-Splash-Induced Spray

In rainy days, due to the effect of load in the process of rolling water film on vehicle tires, the process of forming water mist belongs to compression atomization. This form of atomization is to use compressed air to form high-speed air flow through the small nozzle, and the negative pressure generated will drive the water film to spray on the barrier (tire) together, splashing around under the high-speed impact, so that the droplets become misty particles and eject from the air outlet pipe (the gap between tire and road surface). The water mist generated by the automobile tire passing through the road with water film will absorb and scatter photons, thus affecting the visibility. On the highway, the higher speed also causes the water mist with larger influence range and longer dissipation time. This phenomenon, which is jointly affected by the vehicle and the water film, will actually cause dynamic loss to the driver's visual field, while the traditional roadside visibility meter cannot provide effective early warning and control data support.

The Federal Highway Administration (FHWA) of the United States initially conducted a real vehicle study of tire sputtered water mist in a closed laboratory [6]: assuming that the vehicle sputtered water mist in a fixed space, the vehicle selected a common car model, the study space size was 4.0 m × 2.5 m × 1.6 m, the volume was 16 m3, and the corresponding size range of the surrounding area of the vehicle was 4.4 m × 2.6 m × 1.7 m. the water volume calculation formula of the sidewave (tire side) and the tire wave (directly behind the tire) was as following Equation (8):

$$\begin{aligned} M_T &= vb(1-k)\,h_g\,\gamma_w \\ M_S &= 0.9\gamma_w\,vb(h-kh_f-(1-k)\,h_g) \end{aligned} \tag{8}$$

where v: vehicle speed, m/s; b: tire width, m; h: water film thickness, m; γ_w: water density, kg/m3; M_T and M_S are the water volume of side wave and tire wave, respectively,

kg/s; k: the ratio of the width of the non-groove of the tire tread, taken as 0.75; H_f: thickness of water film brought up by each rotation of tire; and H_g: water film thickness on the tread.

In terms of water-film thickness acquisition, this study adopted an empirical regression model based on experimental results for calculation [22]. The key parameters influencing water-film thickness in this model include the average pavement texture depth, rainfall intensity, and road gradient. It should be noted that texture depth is typically measured using precise techniques such as ground-penetrating radar or the sand-patch method. However, since the present research focuses on evaluating the impact of rain–fog coupling on visibility and driving risk based on a monocular camera, the drainage characteristics of pavement materials were not included in the study scope. Therefore, referring to the typical properties of AC-type asphalt pavement, the texture depth was simplified and assumed to be 1.2 mm [23]. On this basis, the water-film thickness model was further simplified to be dependent only on rainfall intensity and road gradient, and its computation is expressed as Equation (9):

$$WT=0.005979\times MTD^{0.11}\times RAIN^{0.59}\times CSLP^{-0.42}\text{-}MTD \quad (9)$$

where WT: water-film thickness, mm; MTD: average structural depth of road surface, mm; $RAIN$: rainfall intensity, mm/h; and $CSLP$: slope of road surface.

Optically, the strict definition of visibility is the path length through which the luminous flux of the parallel beam emitted by the incandescent lamp is weakened to 5% of the initial value in the atmosphere. Therefore, it is only necessary to carry out the whole process numerical simulation of the path of photons to reduce the number of photons to the path length that can be reached by only 5% of the initial value. For the random behavior of photons in this process, the Monte Carlo method is used to simulate the model study. Each photon will have four possibilities in the scattering process, namely escape, collision, scattering and absorption. This possibility is random and can be defined as the probability density function. At the same time, the collision between photons will change its original trajectory, that is, the numerical simulation of multiple scattering. The simulation model is shown in Figure 3, and the pseudo code of photon motion simulation based on Monte Carlo is shown in Algorithm 1**.**

In this study, the spray cloud is represented as an equivalent monodisperse system, characterized by the Sauter Mean Diameter (SMD) [13]. The scattering characteristic parameters of water-mist particles can be defined using Mie theory [24], including the extinction coefficient K_C, absorption coefficient K_a, scattering coefficient K_s, the scattering phase function $P(\theta)$, and the amplitude functions S_1 and S_2 of the scattered light. In this study, the Monte Carlo simulation of water-mist particle motion is conducted based on the scattering parameters obtained under different vehicle speeds and water-film conditions. The detailed data structure can be found in [13].

As shown in Equation (10), d is the photon transport step [25], which represents the distance a photon travels between two consecutive scattering events.

$$d=-\frac{\ln r_1}{\pi r^2 N_0 K_S} \quad (10)$$

where r_1: a random variable within the interval [0, 1]; r: the radius of a water-fog particle; N_0: the number of water-fog particles per unit volume; φ: the azimuth angle, given by $\varphi=2\pi r_3$; r_3: a random variable uniformly distributed in [0, 1]; θ: the scattering angle,

which can be obtained inversely from $r_4 = \frac{\int_0^{\theta} P(\theta)d\theta}{\int_0^{\pi} P(\theta)d\theta}$; and r_4: a random variable within [0, 1].

Algorithm 1 Simulation algorithm of the fate of a photon

Monte Carlo Photon Simulation Procedure

```
N ← total number of photons
L ← distance from source to detection plane (z = 0)
K_a ← scattering coefficient
K_s ← the scattering phase function
K_c ← extinction coefficient (K_a = Kc + K_s)
count ← 0              // Counter for photons reaching detection plane

for i in range(N):
    z ← L
    while z > 0:
        r1 ← random number in [0, 1]
        if r1 ≤ K_a/K_c:
            // Photon is absorbed
            break
        else:
            // Photon is scattered
            ξ ← random number in [0, 1]
            d ← −ln(ξ)/K_c          // Step length sampled from exponential distribution
            if d > z:
                // Photon escapes before reaching detection plane
                break
            else:
                z ← z–d
                θ, φ ← sample from phase function P(θ)
                // Update photon direction, assuming following Mie theory
                // For simplicity, assume motion remains along -z for now

    if z ≤ 0:
        count ← count + 1
R ← count/N
V ← the minimum L where R ≥ 0.05

return V
```

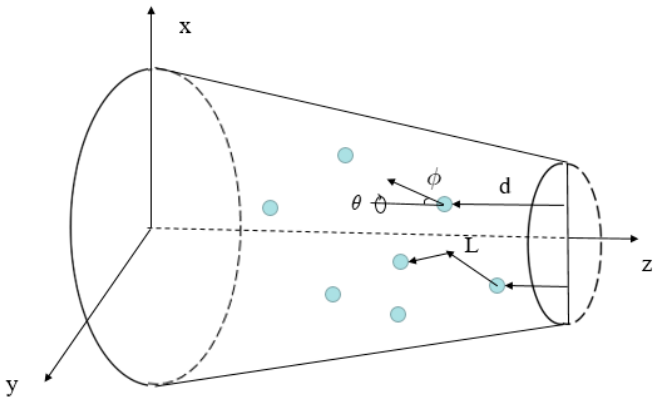

Figure 3. Simulation of photon propagation.

2.4. Dynamic Visibility Coupling and Risk Model

Although from an optical point of view, visibility is usually defined as the path length corresponding to the attenuation of the luminous flux of the parallel beam emitted by the incandescent light source to 5% of the initial value in the process of propagation in the atmosphere [26], in engineering applications (such as highway traffic and airport operation), visibility more often refers to the maximum horizontal distance that normal vision individuals can recognize and distinguish target objects of specific size in the daytime [27]. In this study, the concept of dynamic visibility is introduced to reasonably describe the driving visibility affected by the superposition of regional fog and water fog in front of the vehicle. When the rear vehicle follows closely in the water mist area aroused by the vehicle in front, its visual distance will be significantly reduced due to the local water mist blocking effect; At the same time, if there is a generalized haze background (i.e., global fog) in the external environment, the local visibility will be further limited. Therefore, the dynamic visibility can be regarded as the forward visual range that the driver can actually perceive under the joint action of multi-source visual range obstacles, which has significant spatio-temporal variation characteristics and is significantly affected by the distance from the vehicle in front.

According to the optical experiment of water mist splashed by the truck, the extinction level recovers to a negligible value between 1 and 2 s after the end of the truck crosses the detection line [28]. To incorporate this temporal decay into the model, we convert it into a spatial attenuation term. Assuming the leading vehicle travels at a constant speed v_0, the corresponding decay distance of the water-mist tail can be expressed as $L_d = v_0 \times \Delta t$, where $\Delta t \in [1, 2]$. Consequently, the instantaneous visibility of the following vehicle is not only determined by the Euclidean distance D but also dynamically modulated by the dispersal of the mist tail over time. This spatial–temporal coupling enables the real-time risk evaluation model to capture the transient evolution of visibility under rain–fog coupled conditions. We use uneven extinction in the air to characterize the range of water mist. Assuming that the horizontal distribution of water mist caused by the front vehicle is the same width as the lane (3.75 m), and the longitudinal distribution length of water mist is the speed of the front vehicle, the Euclidean distance between the target vehicle and the end of the front water mist is as following Equation (11):

$$D = \sqrt{(y_s - 2v_0)^2 + x_s^2} \tag{11}$$

where y_s : the longitudinal distance between the vehicle in front and the target vehicle; v_0 : front vehicle speed; and x_s : the lateral distance between the vehicle ahead and the target vehicle.

Further, the dynamic visibility of the target vehicle can be obtained as Equation (12)–(14). According to the AASHTO grade-based stopping sight distance (SSD) formulation [29], the driver's perception–reaction time is assumed to be 2.5 s and the braking deceleration is taken as 3.4 m/s² Given that the roadway grade within the analyzed segment is G = 0 (the studied road length is less than 100 m, and thus the influence of grade is negligible), the SSD expression simplifies to Equation (14).

$$V = (D + V_2)k \tag{12}$$

$$k = e^{\frac{D-ssd}{V_1-ssd}} \tag{13}$$

$$ssd = 2.502v + \frac{v^2}{6.7926 + 19.6G} \tag{14}$$

where V : the dynamic visibility of the target vehicle in the actual road conditions; D : the Euclidean distance between the target vehicle and the rear end of the fog ahead; k: the correction coefficient of dynamic visibility based on global visibility and stopping sight distance; V_2 : visibility within the range of water mist; and V_1 : global visibility.

In order to better describe and identify the risk of driving in the dynamic visibility environment, we refer to the relevant research on the collision risk in the work zone [30], use the safety potential field model [31], and introduce the dynamic visibility to quantify the vehicle collision risk. As shown in Figure 4, in the vehicle safety potential field, the vehicle in front is regarded as the interactive object, and the virtual collision point between the target vehicle and the interactive object in front is defined as the point with the maximum field strength on the contour of the interactive object, which is most likely to be the location where the potential collision occurs.

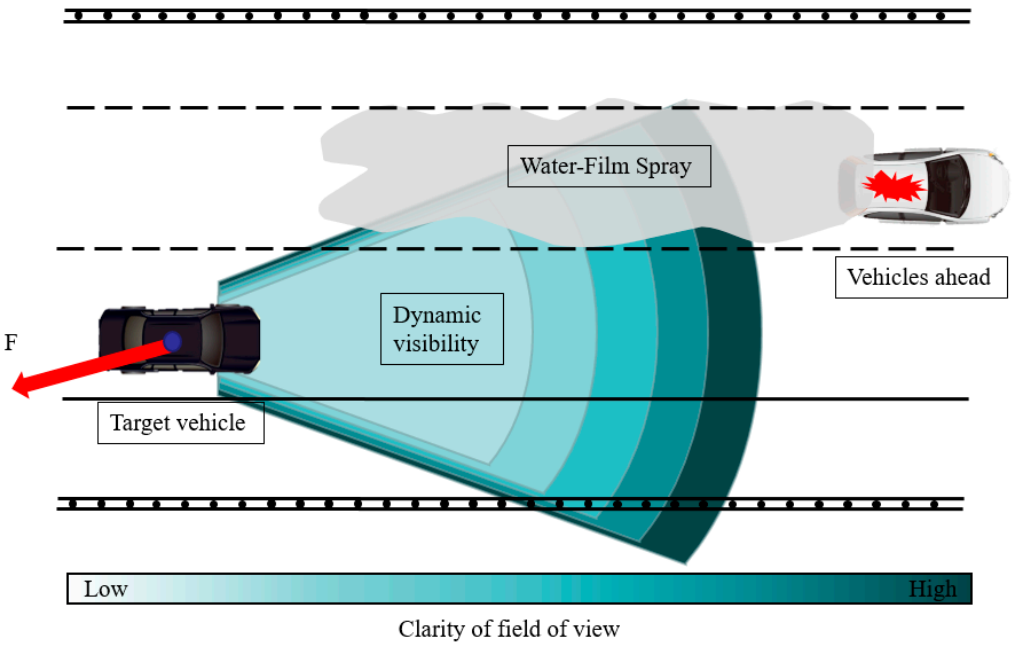

Figure 4. Driver visibility field and risk field force.

As visibility changes, both the distribution pattern and the intensity of the potential field are dynamically adjusted: when visibility decreases, the field gradient becomes steeper, and the local risk force becomes concentrated and propagates forward; when visibility is good, the risk field tends to flatten. To ensure the continuity of the potential field under different visibility conditions, a Sigmoid normalization function is applied to the visibility parameter, allowing the risk intensity to vary smoothly with the degree of visual degradation.

In the model, the field force exerted by surrounding vehicles on the target vehicle is defined as the low-visibility risk field force (LVRFF), and its calculation is given by Equation (15):

$$F = QE = Q\frac{SSD \times V^{-1}}{T^*} = e^{0.125(v-v_0)\cos\phi} \times \frac{\xi v}{\sqrt{y^2 + \xi^2 x^2}} \times ssd \times (D + V_2)^{-1} \times e^{\frac{ssd-D}{V_1 - ssd}} \quad (15)$$

where Q : the risk parameter, representing the relative speed between the target vehicle and the vehicle in front; E : visibility-dependent field intensity term; ssd : stopping sight distance; v : target vehicle speed; v_0 : speed of the preceding vehicle; D : the Euclidean distance between the target vehicle and the rear end of the fog ahead; T^* : the equivalent time-based distance; V : dynamic visibility; ξ : equivalent parameter, depending on the ratio of transverse and longitudinal safety distances; V_2 : visibility within the range of water mist; and V_1 : global visibility.

The definition of the risk correction coefficient in the model is given as Equation (16), As expressed in the exponential term, $Q = e^{0.125(v-v_0)\cos\phi}$, the crash risk increases nonlinearly with both the speed difference and the directional alignment between interacting vehicles. When $\phi \to 0$, $\cos\phi \simeq 1$, and the exponential term dominates, producing a rapid increase in the field force as $v - v_0$ rises.

$$Q = e^{0.125(v-v_0)\cos\phi} \quad (16)$$

The term $E = SSD / V$, Equation (17), defines the visibility-dependent field intensity, which reflects how the dynamic visibility environment modifies the spatial distribution of crash risk. Physically, it represents the ratio between the driver's required stopping sight distance (SSD) and the available dynamic visibility E. When the driver's visual range V approaches or falls below the SSD threshold, the value of increases E sharply, indicating a rapid escalation of potential crash risk.

$$E = SSD / V \quad (17)$$

The speed-dependent correction coefficient is obtained empirically as Equation (18), which comprehensively accounts for both the lateral and longitudinal safety distances. As vehicle speed increases, the weight of lateral risk gradually decreases, and the longitudinal interaction becomes the dominant factor influencing overall risk.

$$\xi = 0.01476 + 0.8v^{-1} \quad (18)$$

This term is introduced to capture the nonlinear amplification effect of reduced visibility on the risk force. As visibility decreases, the exponential component—enhanced by the Sigmoid function—becomes more pronounced, leading to an exponential increase in the overall risk force.

In addition, unlike the Time to Collision (TTC) metric, which considers only longitudinal collisions, the model introduces a vehicle interaction geometric angle parameter in Equation (19).

$$\phi = arctan\frac{y}{\xi x} \tag{19}$$

Based on the geometric interaction angle between vehicles, an equivalent time-based distance T^* is proposed as Equation (20). The equivalent distance decays with speed through the inverse dependence of $\xi = 0.01476 + 0.8v^{-1}$. When v increases from 10 m/s to 30 m/s, δ decreases by nearly 60%, implying that the influence of lateral spacing on total risk weakens while longitudinal distance becomes dominant.

$$T^* = \frac{\xi v}{\sqrt{y^2 + \xi^2 x^2}} \tag{20}$$

3. Results

3.1. Measurement of Visibility Within Spray and Fog Range

When the surveillance camera is exposed to the outside environment, the extinction coefficient K contained in the image is independent of the transmission distance of light in the atmosphere, but related to the visibility distance in the air. The normal visual response threshold of the human eye, that is, the minimum brightness contrast that the human eye distinguishes the target from the background, is 0.02, that is, t (x) = 0.02. On the premise that the actual distance between the road monitoring equipment and the reference object is known, the real-time visibility value in the environment of the monitoring equipment can be estimated only by using the dark primary color prior algorithm to calculate the atmospheric transmittance t of the monitoring video frame.

According to the relevant provisions of the Chinese standard GB 5768-2009 road traffic signs and markings [32], the length of expressway lane line is 6 m, and the distance between two lane lines is 9 m. under the premise of ensuring the pixel accuracy, this paper selects multiple adjacent lane lines as reference objects to process the image, calculates the extinction coefficient, and then obtains the estimated value of global atmospheric visibility. The calculation formula of atmospheric visibility is as follows in Equation (21).

$$V = \frac{ln(t_a / t_b)}{d_{ab}} \tag{21}$$

where V : atmospheric visibility; t_a, t_b: the transmissivity corresponding to the AB two-point pixels in the image; and d_{ab}: the distance between the real physical coordinates corresponding to the two points in the image, which is obtained by reference to the length of the road grid markings and the actual lane lines.

To obtain the observation distance between each point on the road and the camera, we first determine the horizontal distance from the point to the light pole based on its position relative to the 6 m lane markings (with 9 m spacing between markings). Then, using the height of the light pole, we apply trigonometric conversion to calculate the actual distance of the observation point. After obtaining the actual distances of multiple observation points from the camera, along with their corresponding vertical pixel coordinates in the image, we fit the overall distribution relationship to derive a mapping between pixel coordinates and the actual physical distance from the camera for all points in the image. the distance relationship between a point in the road and the camera is shown in Figure 5:

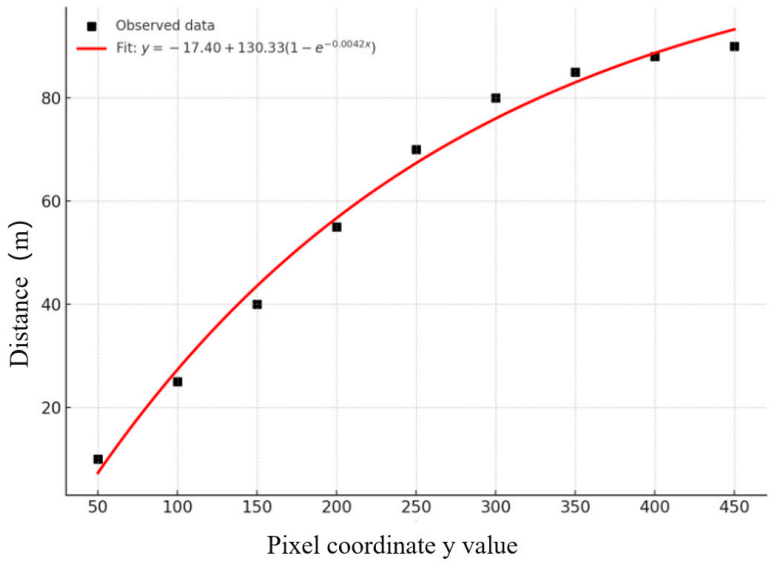

Figure 5. Conversion of Image Pixel Coordinates to Distances between Camera and Observation Points.

Based on the Monte Carlo model, the motion path of photons under different water mist particle number concentrations was calculated, and the vehicle speeds of 60 km/h, 80 km/h and 120 km/h were selected for simulation calculation at the water film thickness of 0.5 mm, 1 mm, 2.5 mm and 5 mm, respectively. Finally, the visibility data under different vehicle speeds and water film thickness are obtained as shown in Figure 6.

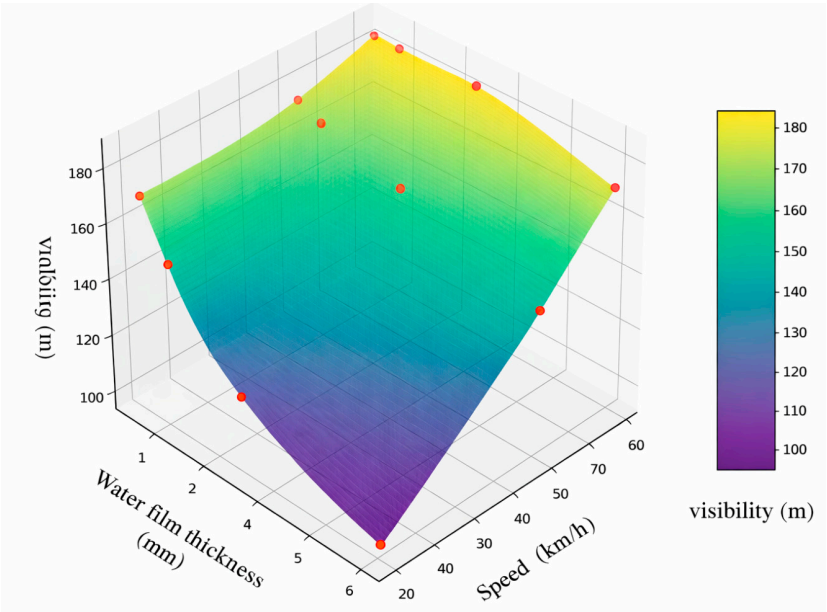

Figure 6. Surface graph of the relationship between visibility, water film thickness, and vehicle speed.

By using Python 3.8's sklearn library to conduct multiple nonlinear regression analysis on the data, the fitting model is as Equation (22).

$$V = 238.942 - 1.028v + 3.637h + 0.004v^2 - 0.201vh + 1.031h^2 \quad (22)$$

where V is the visibility range (m), v is the vehicle speed (km/h), and h is the water-film thickness (mm).

The determination coefficient R^2 = 0.9832 of the model shows that the model can explain 98.23% of the visibility variation. The results of data analysis show that under the condition of fixed water film thickness, the visibility decreases by about 1.402 m on average for every 1 km/h increase in vehicle speed; while under the condition of fixed vehicle speed, the visibility decreases by about 18.094 m for every 1 mm increase in water film thickness. The coefficients of quadratic and interactive terms in the model also show significance, revealing the nonlinear joint effect between vehicle speed and water film thickness, that is, when the vehicle speed is high and the water film is thick, the visibility decreases more significantly. It can be seen that the vehicle speed and water film thickness have a superimposed negative impact on the driving sight distance under the rainfall or road area water environment, which significantly aggravates the driving risk. It is particularly noteworthy that under high-speed driving conditions, the water mist formed between the tire and the wet road surface has a strong blocking effect on the front field of vision. If the distance between the vehicle and the front workshop is small, and the vehicle is in the water mist area aroused by the front vehicle for a long time, the driver's visual range may be rapidly reduced to 200 m or even 100 m, which is far lower than the safe stopping visual distance required for high-speed driving. In addition, the weakening of braking performance on slippery roads will further reduce the vehicle's emergency handling capacity, and it is very easy to induce serious accidents such as rear end collision. Therefore, the spatial position and relative distance of the water mist formed between the vehicle and the vehicle in front have become the key factors affecting the dynamic change in driver's visibility, which should be paid attention to in the actual driving control.

3.2. Driving Risk Distribution Under Low-Visibility Conditions

Figure 7 shows the scatter distribution and fitting curve between the low-visibility risk field force F and dynamic visibility V and shows that F decreases significantly with the increase of V (the slope of the fitting curve is significantly less than zero, $R^2 \approx 0.6$, $p < 0.001$), indicating that the proposed index can sensitively and accurately reflect the impact of real-time visibility changes on driving risk. According to Rating of early-warning of road traffic under fog weather conditions [33], 200 m is the visibility control threshold, and about 18% of the observation points in this sample (scattered points are located in the shadow area of v < 200 m) need to implement speed limit or control measures; The F corresponding to these low visibility periods are generally high, which further verifies the response ability of the risk indicators to the situation of insufficient visibility. The orange mark indicates the stopping sight distance (SSD) at which the current dynamic visibility is lower than the corresponding speed—this kind of sample accounts for about 12% of the total—and its F value is higher than that of the SSD satisfaction group under the same V condition, indicating that the risk increases significantly when the stopping sight distance is insufficient. On the other hand, only about 4% of the observation points have v > 470 m (i.e., they are not disturbed by the water mist splashed by the vehicle in front), and the corresponding F is the lowest and the distribution is the most concentrated, which proves the interference effect of the water mist splashed by the vehicle in front on road visibility and its adverse impact on driving safety.

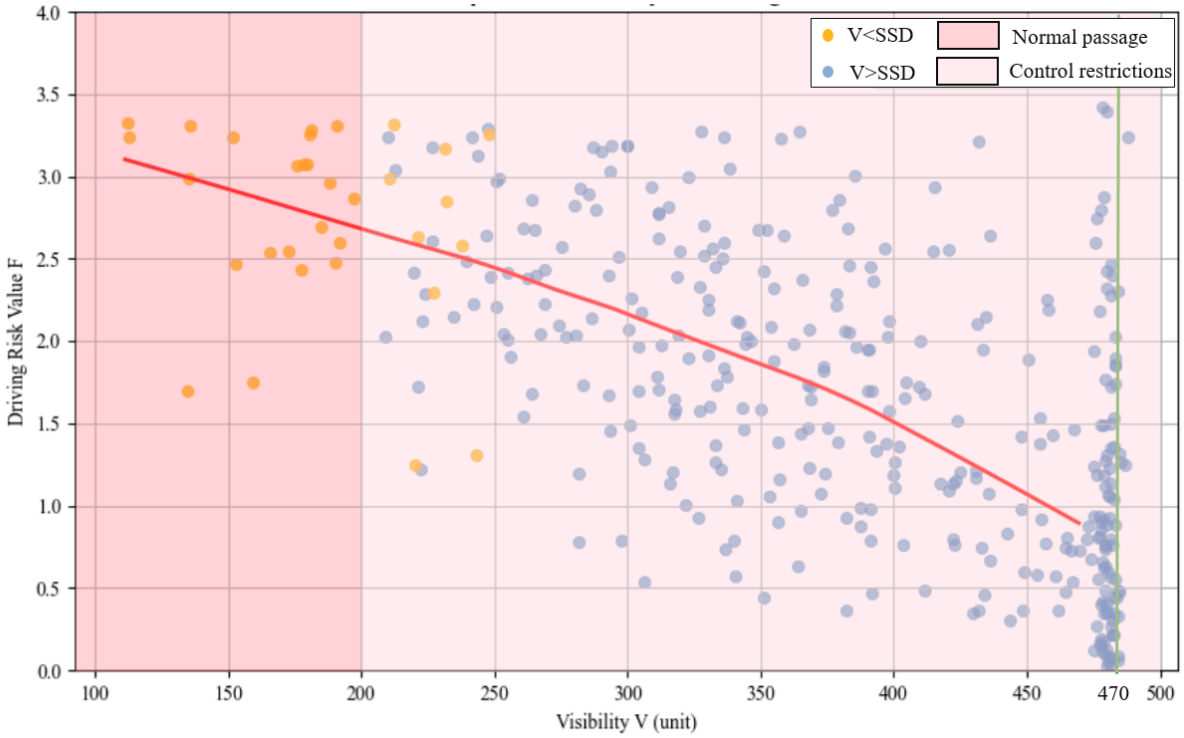

Figure 7. Distribution of the Low-Visibility Risk Field Force.

By observing the high-risk vehicles in the video, we found that they can be roughly divided into two situations: as shown in Figure 8, the target vehicle approaches the water mist caused by the vehicle in front during driving and keeps a certain following distance from the vehicle in front; in another case, as shown in the figure, the target vehicle is overtaken, and when the overtaking vehicle exceeds the target vehicle it begins to be affected by water spray.

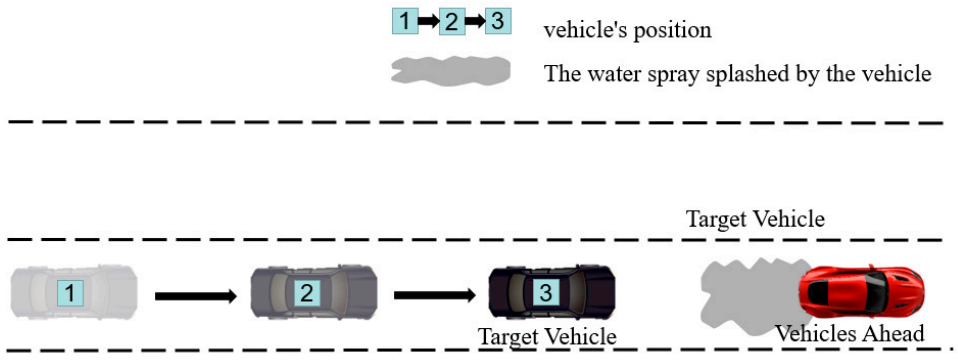

(**a**) The target vehicle follows the vehicle ahead

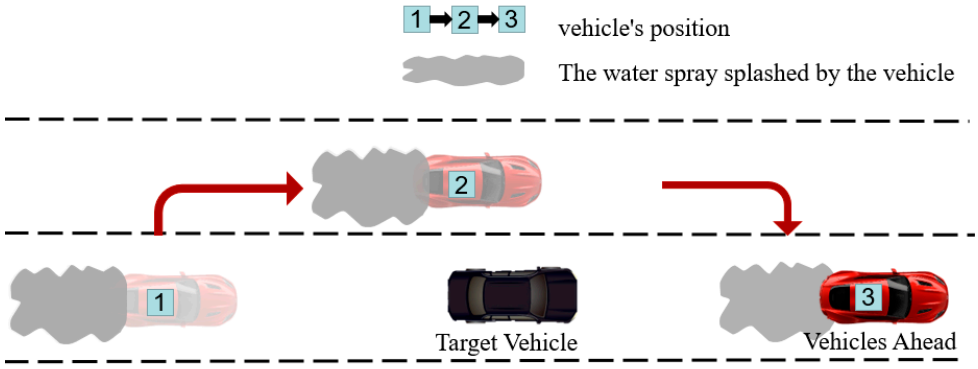

(**b**) The target vehicle is overtaken by vehicle ahead

Figure 8. High-risk driving scenarios.

Figure 9 shows the box diagram comparison of the risk F under the two driving scenarios of following and overtaking under the interference of low visibility. In the car following situation, the median of F is about 2.57, the interquartile distance (IQR) is about 0.36 and the whisker range is about 2.25 to 2.99, indicating that the risk distribution is relatively concentrated and there is no extreme outlier. In contrast, in the case of being overtaken, the median F rose to about 3.23, and the IQR narrowed to about 0.14, but the whisker extended outward to about 2.99 to 3.42.

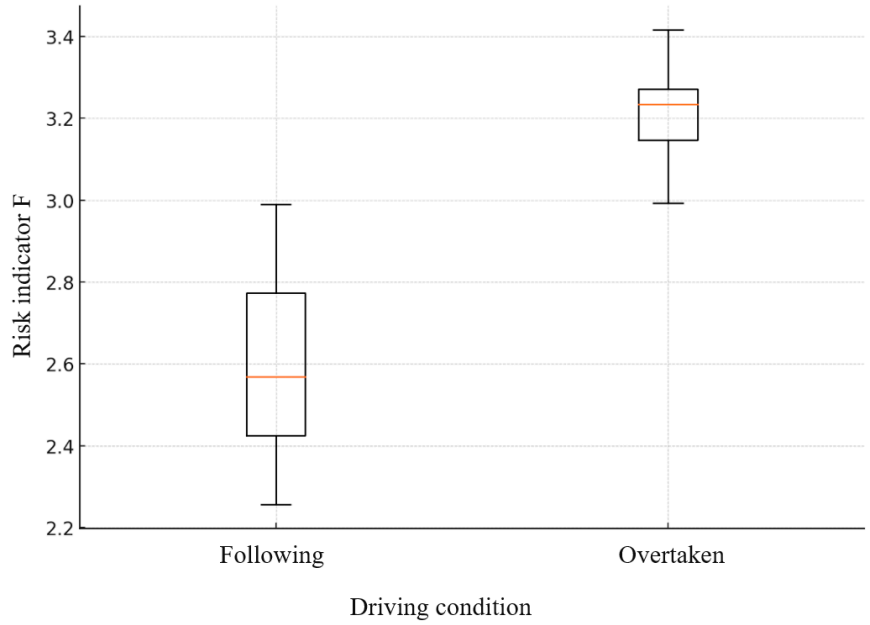

Figure 9. Distribution of potential field forces in following and overtake states overtaking introduces more pronounced fluctuations in instantaneous risk and a tendency toward higher-risk states. This difference arises from the distinct visibility dynamics between the two scenarios. During following, drivers tend to maintain a more consistent headway, which limits rapid changes in dynamic visibility and mitigates the influence of spray generated by the preceding vehicle. During overtaking, however, the higher relative speed and reduced lateral clearance cause a sharper decline in visibility. Moreover, because spray-induced extinction dissipates with a delay, the target vehicle remains exposed to degraded visibility for a longer duration even after the overtaking maneuver is completed.

Overall, the dispersion patterns and tail behavior of F across the two scenarios demonstrate that overtaking under limited visibility produces substantially higher transient risk compared with stable following. These findings quantitatively validate the sensitivity of the proposed LVRFF metric in distinguishing risk levels associated with different driving behaviors in low-visibility conditions.

4. Discussion

In practical applications, it is essential to clarify how roadway images captured by external CCTV cameras correspond to the visual experience of the driver inside the vehicle. Although the camera is mounted above the road, the geometric transformation established through camera calibration enables each pixel in the surveillance image to be mapped to its corresponding real-world position and distance. By further converting atmospheric transmittance into extinction coefficients and visibility values, the system approximates the forward sight distance that a driver would perceive along the same roadway segment. Thus, the externally captured images provide a reliable surrogate representation of the driver's actual visibility field, allowing the dynamic visibility model to reflect both global fog conditions and localized spray interference encountered by the following vehicle.

From an engineering perspective, the proposed method can be integrated into existing highway infrastructure through roadside CCTV networks and centralized traffic management platforms. Once the real-time visibility deteriorates below the predefined thresholds, the system can automatically trigger warnings delivered through variable message signs (VMS), in-vehicle navigation systems, or connected-vehicle communication modules (e.g., LTE-V/5G). This provides drivers with timely speed adjustment or lane-change advisories, enhancing safety under adverse weather conditions.

4.1. Accuracy Verification of the Channel Prior-Based Dehazing Method

After calculation, the air perspective rate based on the dark channel prior algorithm is obtained, and then the visibility of CCTV images taken in this period is obtained. The sampling is carried out every five minutes, and compared with the data measured by the visibility meter provided by the highway operation management department and the visibility analytic value of the official image.

To rigorously verify the accuracy of this visibility measurement method and its robustness under different road environments and visibility conditions, this study selected a rain and fog weather event on 14 September 2023, as the observation scenario. Visibility identification and analysis were conducted using data from four surveillance cameras along the PL Highway. The sampling period covered the entire rainfall process. This regional rainfall was accompanied by the formation and development of fog. As the rain intensity shifted from moderate to light, visibility gradually improved, and the fog condition weakened from dense to light. For accuracy verification and comparison, visibility observation data from fixed meteorological stations along the highway, as well as visibility data provided by local weather stations, were simultaneously collected. Based on the information provided in the image, this study has classified visibility levels according to the visual requirements for vehicle driving as follows:

(1) Good (G): Visibility greater than 10 km.
(2) Fair (K): Visibility between 5 km and 10 km.
(3) Moderate (M): Visibility between 2 km and 5 km.
(4) Poor (N): Visibility between 0.5 km and 2 km.
(5) Very Poor (P): Visibility between 0.2 km and 0.5 km.
(6) Extremely Poor (Q): Visibility less than 0.2 km.

The distribution of surveillance cameras and the sources of meteorological data are as following Table 1 and Figure 10.

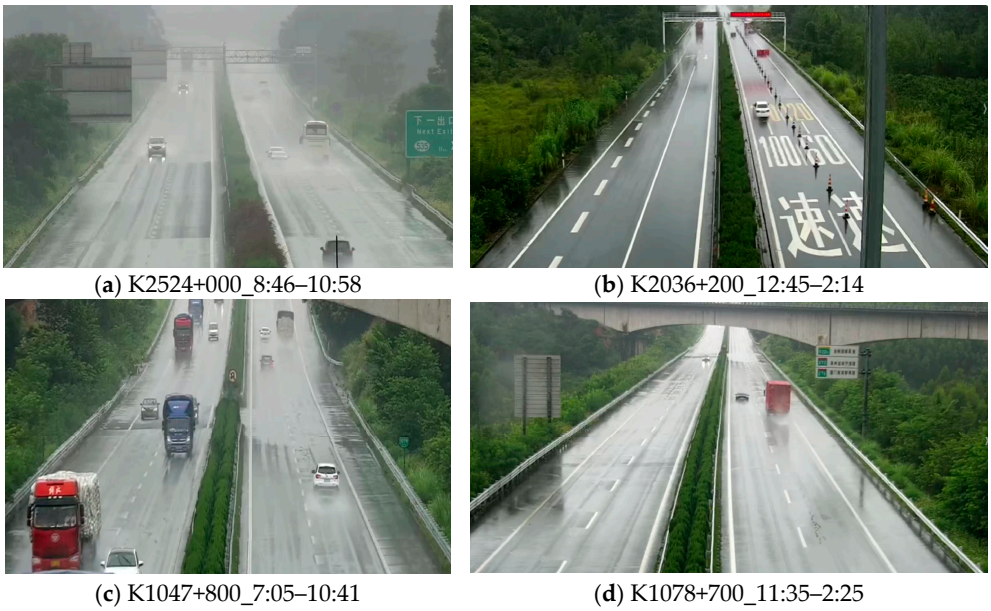

(**a**) K2524+000_8:46–10:58 (**b**) K2036+200_12:45–2:14

(**c**) K1047+800_7:05–10:41 (**d**) K1078+700_11:35–2:25

Figure 10. Video Overview of Rainfall and Fog.

Table 1. CCTV Information.

Station Number	Time	Average Hourly Rainfall (mm/h)	Average Hourly Visibility (m)	Fog Grade	Road Grade (%)
K2524+000	8:46–10:58	12.6	184.5	Extremely Poor (Q)	0.5
K2036+200	12:45–14:14	9.4	648.0	Poor (N)	0.8
K1047+800	7:05–10:41	3.3	405.9	Very Poor (P)	1.5
K1078+700	11:35–14:25	1.2	512.1	Poor (N)	1.6

To verify the reliability of the dark channel prior algorithm combined with camera parameter calibration among similar physical model-based approaches, this study also adopts the Canny edge detection horizon method for comparison [34]. The method estimates the extinction coefficient of fog and subsequently derives the visibility distance by analyzing the horizon position and vertical luminance variation in road scenes. The core idea is that, under foggy conditions, the luminance contrast of distant objects decays exponentially with increasing distance; therefore, the vertical luminance gradient in the image can be used to infer fog density and visible range. The algorithm first applies the Canny–Deriche operator to extract image edge features and determines the horizon position through Hough transform combined with RANSAC fitting, thereby achieving geometric calibration between the road plane and camera perspective. Under the flat-world assumption, the vertical image coordinates are then mapped to real-world distances. By computing the row-wise luminance variation curve of the road region, the algorithm identifies the inflection point where the luminance gradient changes abruptly—corresponding to the visual boundary of the fog layer. Finally, according to the Koschmieder atmospheric scattering model, the extinction coefficient of fog is estimated, from which the visibility distance is calculated.

The highway operating unit uses a roadside infrared forward-scatter visibility sensor. The model of this sensor is DNQ1. Its core principle is to calculate the meteorological

optical range (MOR), i.e., visibility, by measuring the scattering intensity of infrared light by suspended particles in the air (such as fog, haze, rain, and smoke) to derive the atmospheric extinction coefficient. It consists of an optical transmitter, an optical receiver, and a microprocessor controller. The transmitter emits infrared light pulses, while the receiver simultaneously detects the intensity pulses of light scattered by atmospheric particles. All information is collected by the measurement microcontroller. The operational data of the instrument are shown in Table 2:

Table 2. Visibility sensor parameters.

Monitoring Range (km)	Accuracy	Frequency (Hz)	Scattering Angle Range (°)	Peak Wavelength (nm)	Bandwidth (nm)
5~8	95%	1	39~51	850	100

Combining the meteorological conditions in Table 1 with the comparative results in Figure 11a–d, it can be observed that the dark channel prior algorithm maintains good stability and robustness in visibility estimation under different rainfall intensities and fog levels.

In the time period at station K2524+000, when the average hourly rainfall was 12.6 mm and visibility was only 184.5 m (fog level: poor, n), the algorithm still stably output results with a standard deviation of 34.7 m and an accuracy of 86% (compared to sensor data), almost consistent with the infrared forward scatter sensor data, with maximum fluctuations below ±40 m. In contrast, the meteorological station data showed severe oscillations (500 m–2500 m). When the rainfall decreased to 9.4 mm and visibility improved to 648 m (fog level: good, k), with noticeable changes in the observation interval, the algorithm's estimated values increased synchronously, showing a trend consistent with the sensor control group and indicating its effective response to changes in atmospheric transmittance.

Similarly, in the time periods 7:05–10:41 and 11:35–14:25, the average hourly rainfall was 3.3 mm and 1.2 mm, with visibility values of 405.9 m and 512.1 m, corresponding to fog levels "fair (m)" and "good (k)", respectively. Under these conditions, the results of the dark channel prior algorithm remained highly consistent with the infrared sensor data, with errors controlled within ±60 m and strong data robustness. The standard deviation of the algorithm remained low, whereas the meteorological station observations still exhibited significant random fluctuations.

Furthermore, the comparison revealed that both the infrared forward scatter sensor and the dark channel prior algorithm showed larger data fluctuations under average hourly rainfall of 9.4 mm and 12.6 mm compared to lower rainfall conditions, with standard deviations reaching 67.8 m. The working principle of the sensor involves measuring the forward-scattered light intensity of infrared radiation by suspended particles (such as raindrops, fog droplets, dust, etc.) in a small spatial area between the transmitter and receiver. The speculated reasons for data disturbances may include lens contamination caused by raindrops adhering to the sensor lens and surveillance camera lenses, secondary effects such as splashing water and spray accompanying rainfall, and the heterogeneous nature of convective heavy rainfall, which further interferes with visibility recognition in the current area.

Overall, in the observational experiments at the station locations, the dark channel prior algorithm accurately captured visibility trends under four different rainfall levels (1.2–12.6 mm) and visibility ranges (184.5–648 m), demonstrating significant noise resistance. Compared to the discrete errors in meteorological station data caused by localized precipitation, light conditions, and fog droplet scattering, the algorithm effectively

eliminates brightness drift effects under mixed rain–fog conditions by extracting the reflectance of dark pixels in non-sky regions based on optical principles. Thus, it exhibits higher stability and engineering applicability in all-weather visibility estimation. Moreover, meteorological station data struggle to provide effective visibility predictions for multiple sections along the entire highway, whereas densely deployed surveillance cameras enable meteorological condition analysis at a 1 km segment level.

In comparison with the visibility data obtained using the Canny edge detection method, the dark channel prior algorithm demonstrated higher robustness across all four scenarios. The Canny-based approach achieved relatively high accuracy on segments K2524+000 and K2036+200, reaching 91% and 86%, respectively. However, on segments K1047+800 and K1078+700, the presence of overhead structures and the concave curvature of the roadway caused inconsistent edge responses at block boundaries, leading to blocking artifacts and greater deviations in visibility estimation. These results indicate that the dark channel prior algorithm possesses superior deployability and adaptability for diverse detection scenarios.

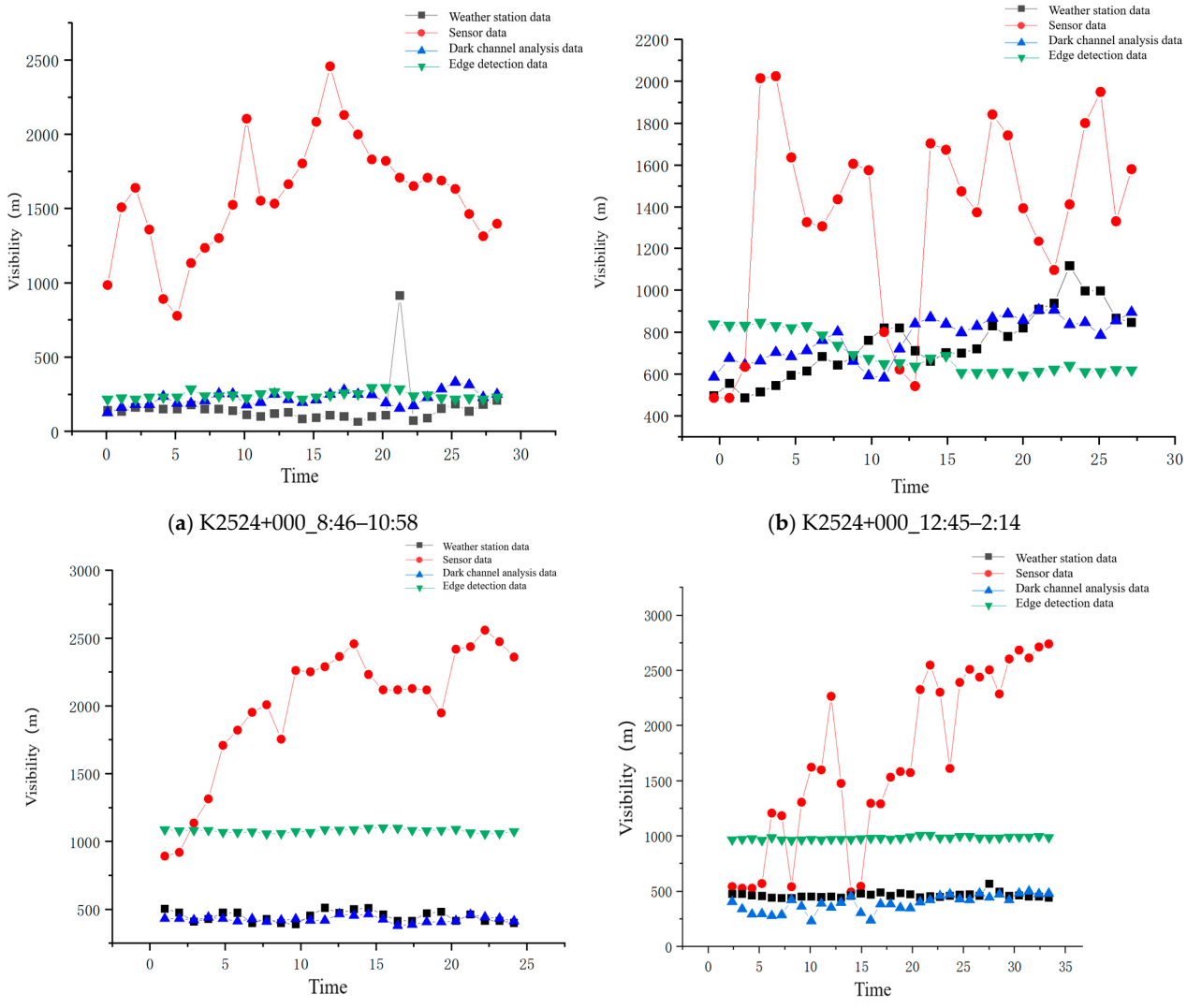

(**a**) K2524+000_8:46–10:58

(**b**) K2524+000_12:45–2:14

(**c**) K1078+700_7:05–10:41

(**d**) K1078+700_11:35–2:25

Figure 11. Comparison of visibility data based on dark channel prior algorithm, meteorological stations, and laser sensors.

4.2. Risk Analysis of a Visibility-Based Safety Potential Field

Surrogate Safety Measures (SSMs) serve as primary quantitative indicators for microscopic collision risk. They assess the likelihood of a vehicle collision by evaluating the temporal and spatial proximity between a vehicle and an obstacle [35]. An event where the proximity exceeds a specific threshold is defined as a traffic conflict. SSMs are categorized into deceleration-based measures and time–proximity-based measures. Among deceleration-based surrogate safety measures, the Deceleration Rate to Avoid a Collision (DRAC) is one of the most prominent representatives [36]. It is defined as the minimum deceleration required for a following vehicle to avoid a collision with a leading vehicle, assuming the leading vehicle maintains a constant speed while the following vehicle brakes with a certain deceleration.

Time–proximity-based surrogate safety measures, which comprehensively consider vehicle speed and spatial distance, can more accurately assess driving risks. Representative indicators in this category include Time to Collision (TTC) [35] and Time to Accident (TA) [37]. TTC is defined as the remaining time before two vehicles collide if they maintain their current speeds and directions. However, both TTC and DRAC are only applicable in scenarios where the speed of the following vehicle is greater than that of the leading vehicle. This limitation implies that TTC and DRAC have constraints in evaluating collision risks in emergency braking situations. To address this, some researchers have proposed TA as an evaluation metric, defined as the time required for the following vehicle to reach the position of the leading vehicle. The key difference between TA and TTC lies in the assumption that in TA, the following vehicle maintains a constant speed while the leading vehicle performs emergency braking.

The driving risk indicator F derived from risk field theory requires further comparison with traditional safety surrogate measures. This study extracted vehicle trajectories from surveillance data under foggy and non-foggy conditions, calculating three conflict indicators—TTC, TA, and DRAC—as well as the driving risk indicator F. The statistical distributions of these four vehicle risk indicators under normal visibility (visibility < 200 m) and good visibility (visibility > 500 m) are shown in Figure 12. The following trends can be observed:

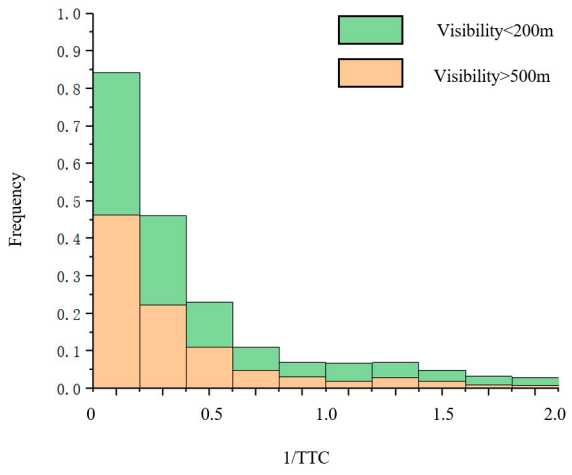

(**a**) Frequency distribution of 1/TTC

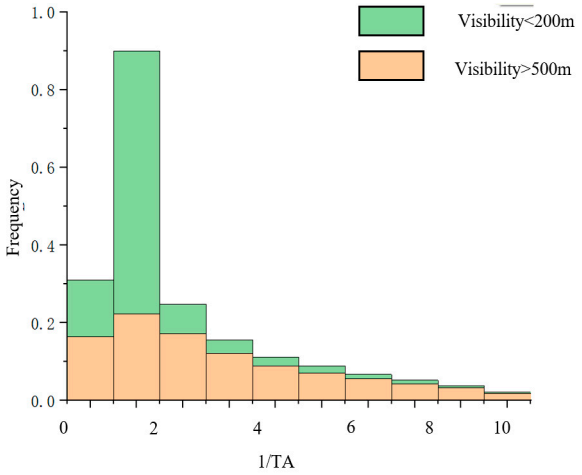

(**b**) Frequency distribution of 1/TA

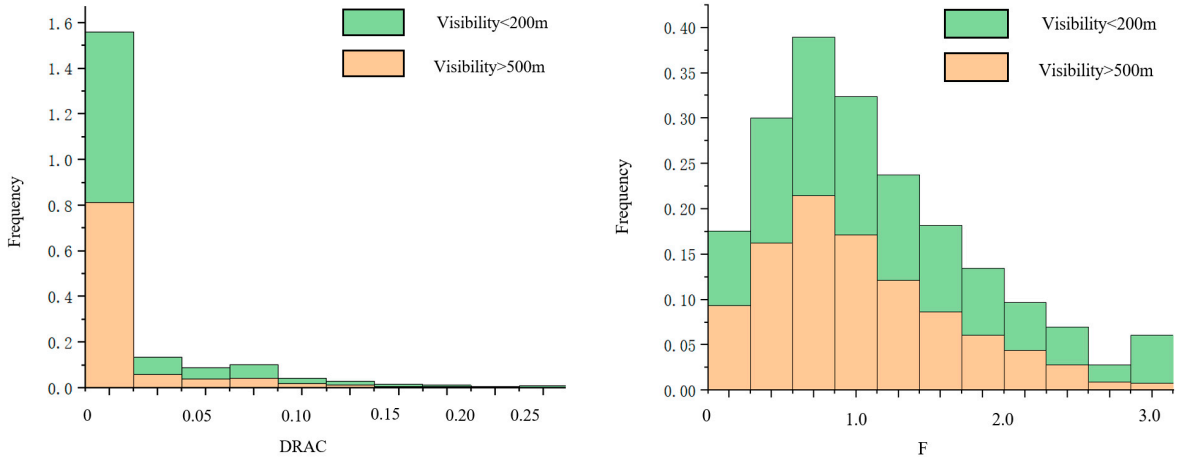

(**c**) Frequency distribution of 1/DRAC (**d**) Frequency distribution of F

Figure 12. Frequency distribution of four risk conflict indicators under two visibility levels.

The DRAC threshold is –3.4 m/s² [38], and the TTC threshold is 3 s (i.e., the 1/TTC threshold is 0.33 s^{-1}) [39]. In the study samples, both TTC and DRAC values were below their respective thresholds under both foggy and normal weather conditions, indicating their low sensitivity to collision risk. This makes them inadequate for characterizing real-time risk conditions during risk monitoring, and they are only suitable as quantitative measures of overall risk over longer time frames.

The driving risk indicator F demonstrates significantly better discriminative ability compared to the other three conflict indicators. When integrated with the risk field model that accounts for dynamic sight distance, F effectively enhances sensitivity to risk factors such as relative speed, following distance, and visibility—a critical meteorological factor—under low-visibility conditions.

Reduced visibility and rainfall significantly increase the risks associated with routine car-following and lane-changing maneuvers. However, traditional TTC, DRAC, and TA indicators struggle to provide sensitive risk discrimination when meteorological conditions change. Calculations based solely on vehicle acceleration changes and relative positioning fail to identify high-risk behaviors when the driver's sight is obstructed. As shown in Figure 13, a comparison of visibility while following a preceding vehicle under rainy-foggy conditions versus normal conditions reveals that spray kicked up by vehicles traveling at high speeds severely impairs the driver's observation of the road ahead. The driving risk indicator F effectively couples the additional visibility reduction caused by preceding vehicle spray with the existing fog, thereby directly quantifying the collision risk with the vehicle ahead at the current speed. Consequently, it holds significant advantages for identifying risky driving in adverse weather. Moreover, the model also incorporates considerations of vehicle interactions captured by indicators like TTC and TA, making it more comprehensive and reliable for broader applications.

Recent studies have also emphasized that relying on a single surrogate safety measure (SSM) may provide an incomplete representation of crash risk [40]. To address this limitation, the present study does not rely solely on one SSM; instead, the proposed LVRFF index integrates dynamic visibility, relative speed, and geometric interaction factors into a unified risk-field formulation. This approach, although not based on PCA, effectively captures the multidimensional nature of driver risk perception under coupled rain–fog conditions and therefore meets the same objective of fusing heterogeneous risk indicators into a more comprehensive metric.

Figure 13. Comparison of the impact of the presence or absence of water spray on driver visibility.

As shown in Figure 14, four time periods with similar visibility conditions (400 m < visibility < 600 m) but different traffic densities were selected for analysis. The Low-Visibility Risk Field Force (LVRFF) of vehicle samples within each period was computed. The results indicate that the average LVRFF under higher traffic volumes is greater than that under lower traffic volumes, demonstrating that dense traffic flow increases collision risk due to spray-induced visual occlusion.

Meanwhile, the standard deviation of LVRFF in period b (2.80) is higher than that in period a (2.68). This is because, in denser traffic conditions, vehicles tend to adopt more conservative driving strategies after speed reduction, rather than frequent overtaking or close following. In contrast, during period b, the smaller total number of recorded interactions includes several overtaking maneuvers that sharply reduced headway time, thereby increasing the dispersion of LVRFF.

Compared with the quantitative assessment of overtaking and following risks shown in Figure 9, LVRFF proves to be more effective for identifying risky driving behaviors under low-visibility conditions, providing a finer basis for setting minimum safe following distances and maximum speed limits to prevent crashes caused by adverse weather such as rain and fog.

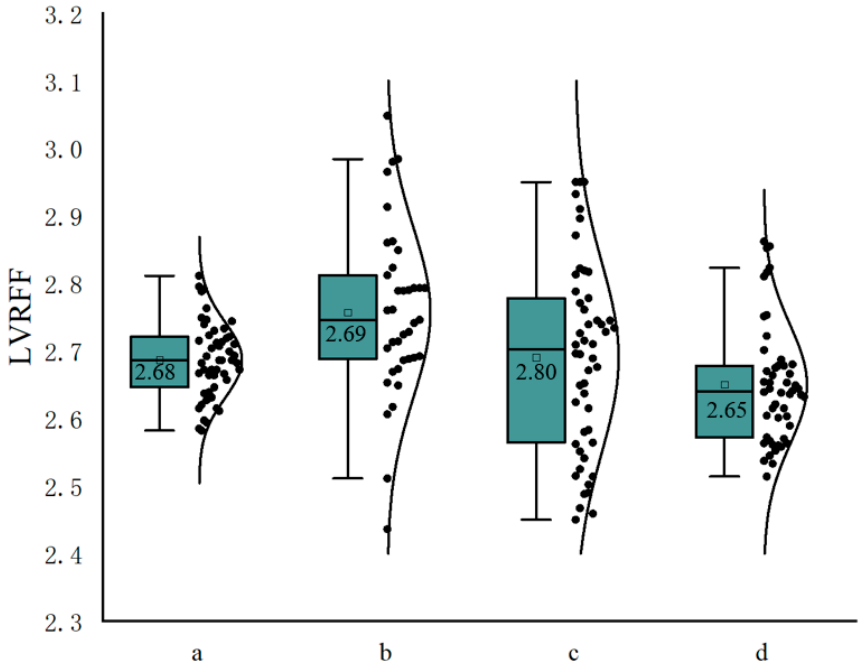

Figure 14. Comparison of LVRFF Trends under Different Traffic Densities**.** a: 87 veh/15 min, b: 62 veh/15 min, c: 54 veh/15 min, d: 50 veh/15 min.

The results obtained in this study demonstrate the quantitative advantages of the proposed Low-Visibility Risk Field Force (LVRFF) in capturing transient risk under rain–fog conditions. Compared with traditional surrogate safety measures such as TTC, TA, and DRAC, LVRFF exhibits substantially higher sensitivity to visibility degradation, especially in scenarios where spray-induced occlusion plays a dominant role. Across the analyzed datasets, LVRFF identified approximately 2–3 times more high-risk events when visibility fell below 200 m, reflecting its capability to integrate dynamic visibility, inter-vehicle distance, and relative speed into a unified risk indicator. Furthermore, LVRFF effectively distinguishes risk variations across different traffic densities, where the medium-density condition—characterized by frequent overtaking and abrupt headway changes—shows significantly elevated risk values compared with high-density flow. These quantitative findings confirm that LVRFF provides a robust and responsive metric for evaluating driving risk in adverse weather, offering meaningful implications for real-time traffic management and visibility-based warning systems.

From the perspective of sustainable transportation, this study provides a practical solution for enhancing highway safety and operational resilience under adverse weather conditions. By leveraging existing roadside CCTV infrastructure, the proposed dynamic visibility recognition and risk assessment framework avoids the need for additional energy-intensive sensing equipment, thereby reducing deployment cost and maintenance burden. The ability to deliver real-time, section-level visibility and risk information supports long-term, data-driven traffic management strategies, contributing to safer, more reliable, and sustainable highway operations.

Author Contributions: Methodology, Z.X., D.W. and X.Y.; Software, Y.Z.; Resources, D.W.; Data curation, C.Z. and X.Y.; Writing—original draft, Z.X.; Writing—review & editing, C.Z. and Y.Z.; Visualization, Z.X. All authors have read and agreed to the published version of the manuscript.

Funding: This work was supported by Fundamental Research Funds for the Central Universities, CHD (300102215206), the Science and Technology Project of Sichuan Transportation Department (2023-A-04), the Science and Technology Project of Sichuan Transportation Department (2021-ZL-15, 2022-ZL-04), and the National Natural Science Foundation of China (72371036).

Institutional Review Board Statement: Not applicable.

Informed Consent Statement: Not applicable.

Data Availability Statement: The datasets presented in this article are not readily available because non-public expressway surveillance data.

Conflicts of Interest: The authors declare no conflict of interest.

References

1. China Climate Change Center. *Blue Book on Climate Change in China (2025)*; Science Press: Beijing, China, 2025.
2. Guo, W.J.; Guo, R.; Xu, Z.L.; Liu, Z.X.; Ding, B.; Wu, D.; Wang, Y.F.; Li, M.Q.; Huang, Y.P. Estimating visibility via differential regression network. *Multimed. Syst.* **2024**, *30*, 365. https://doi.org/10.1007/s00530-024-01556-w.
3. Lu, H.P.; Chen, M.Y.; Kuang, W.B. The impacts of abnormal weather and natural disasters on transport and strategies for enhancing ability for disaster prevention and mitigation. *Transp. Policy* **2020**, *98*, 2–9. https://doi.org/10.1016/j.tranpol.2019.10.006.
4. Jiang, J.Q.; Ketabdari, M.; Crispino, M.; Toraldo, E. Estimating vehicle braking distance over wet and rutted pavement surface through back-propagation neural network. *Results Eng.* **2024**, *21*, 101686. https://doi.org/10.1016/j.rineng.2023.101686.
5. Peng, J.; Chu, L.; Fwa, T.F. Determination of safe vehicle speeds on wet horizontal pavement curves. *ROAD Mater. Pavement Des.* **2021**, *22*, 2641–2653. https://doi.org/10.1080/14680629.2020.1772350.

6. Flintsch, G.W.; Tang, L.; Katicha, S.; de Leon, E.; Viner, H.; Dunford, A.; Nesnas, K.; Coyle, F.; Sanders, P.; Gibbons, R.; et al. Splash and Spray Assessment Tool Development Program. 2014. Available online: https://vtechworks.lib.vt.edu/items/128c8e73-fe7b-4504-a783-44fa5fdc7e30 (accessed on 29 October 2025).
7. Zhang, C.L.; Sun, T.; Chen, J.R.; Li, P.C. A Visibility Monitoring System Utilizing Roadside Video Camera Facilities for Highway Systems. In Proceedings of the 2017 3rd International Conference on Information Management (ICIM 2017), Chengdu, China, 21–23 April 2017; IEEE: New York, NY, USA, 2017; pp. 486–490.
8. Xiao, P.F.; Zhang, Z.D.; Luo, X.C.; Sun, J.Q.; Zhou, X.C.; Yang, X.X.; Huang, L. Highway Visibility Estimation in Foggy Weather via Multi-Scale Fusion Network. *Sensors* **2023**, *23*, 9739. https://doi.org/10.3390/s23249739.
9. Li, W.; Yang, X.K.; Chen, X.T.; Xu, D.; Assoc Computing, M. Attention-based BiLSTM-CNN network for highway visibility prediction. In Proceedings of the 2023 7th International Conference on Electronic Information Technology and Computer Engineering, EITCE 2023, Xiamen, China, 20–22 October 2023; pp. 523–528.
10. Sun, Y.B.; Tang, J.H.; Liu, Q.S.; Zhang, Z.D.; Huang, L. Highway Visibility Level Prediction Using Geometric and Visual Features Driven Dual-Branch Fusion Network. *IEEE Trans. Intell. Transp. Syst.* **2024**, *25*, 9992–10004. https://doi.org/10.1109/TITS.2024.3362905.
11. He, Y.; Ding, J.; Teng, H.Q.; Han, X.F.; Chen, Y.Y.; Zhou, W.J. Visibility detection and prediction of foggy highway based on lane line detection and Winters additive model. In Proceedings of the 2021 40th Chinese Control Conference (CCC), Shanghai, China, 26–28 July 2021; pp. 7254–7259.
12. Qu, Q.L.; Zhang, F.; Liu, P.Q.; Agarwal, R.K. Numerical Simulation of Water Spray Caused by a Rolling Airplane Tire. *J. Aircr.* **2016**, *53*, 182–188. https://doi.org/10.2514/1.C033276.
13. Wang, S.Y.; Chen, T.H.; Yu, B.; Sun, Y.; Qin, X.C. Coupling impacts of spray and rainfall on road visibility and vehicle speeds: A simulation-based analysis. *Can. J. Civ. Eng.* **2022**, *49*, 1220–1230. https://doi.org/10.1139/cjce-2021-0402.
14. Radovich, C.; Plocher, D. Experiments on Spray from a Rolling Tire. In *The Aerodynamics of Heavy Vehicles II: Trucks, Buses, and Trains*; Browand, F., McCallen, R., Ross, J., Eds.; Springer: Berlin/Heidelberg, Germany, 2009; pp. 403–417.
15. Do, M.T.; Edjeou, W.; Riahi, E.; Gennesseaux, M.; Cerezo, V. An Exploitation of Spray Mechanisms to Estimate Water Depths on a Road Surface. In Proceedings of the 10th International Conference on Maintenance and Rehabilitation of Pavements, MAIREPAV-10, Guimaraes, Portugal, 24–26 July 2024; Volume 2, pp. 39–48.
16. Zhang, X.; Feng, Y.; Angeloudis, P.; Demiris, Y. Monocular Visual Traffic Surveillance: A Review. *IEEE Trans. Intell. Transp. Syst.* **2022**, *23*, 14148–14165. https://doi.org/10.1109/TITS.2022.3147770.
17. Kanhere, N.K.; Birchfield, S.T. A Taxonomy and Analysis of Camera Calibration Methods for Traffic Monitoring Applications. *IEEE Trans. Intell. Transp. Syst.* **2010**, *11*, 441–452. https://doi.org/10.1109/TITS.2010.2045500.
18. Steffens, C. Measurement of Visibility by Photographic Photometry. *Ind. Eng. Chem.* **1949**, *41*, 2396–2399. https://doi.org/10.1021/ie50479a015.
19. Dumont, E.; Cavallo, V. Extended Photometric Model of Fog Effects on Road Vision. *Transp. Res. Rec.* **2004**, *1862*, 77–81. https://doi.org/10.3141/1862-09.
20. Hautiére, N.; Tarel, J.-P.; Lavenant, J.; Aubert, D. Automatic fog detection and estimation of visibility distance through use of an onboard camera. *Mach. Vis. Appl.* **2006**, *17*, 8–20. https://doi.org/10.1007/s00138-005-0011-1.
21. Tan, R.T. Visibility in bad weather from a single image. In Proceedings of the 2008 IEEE Conference on Computer Vision and Pattern Recognition, Anchorage, AK, USA, 23–28 June 2008; pp. 1–8.
22. Wambold, J.C.; Henry, J.J.; Hegmon, R.R. Evaluation of pavement surface texture significance and measurement techniques. *Wear* **1982**, *83*, 351–368. https://doi.org/10.1016/0043-1648(82)90189-2.
23. Yang, E.H.; Chen, Q.; Li, J.; Di, H.B.; Huang, B.; Qiu, Y.J. SurfaceTextureReconstructionandMeanTextureDepth Prediction Model of Asphalt Pavement. *China J. Highw. Transp.* **2023**, *36*, 14–23. https://doi.org/10.19721/j.cnki.1001-7372.2023.06.002.
24. Dave, J.V. Scattering of Visible Light by Large Water Spheres. *Appl. Opt.* **1969**, *8*, 155–164. https://doi.org/10.1364/AO.8.000155.
25. Yu, B.; Sun, Y. Simulation of Impact of Water-Film Spray on Visibility. *J. Transp. Eng. Part B Pavements* **2018**, *144*, 04018054. https://doi.org/10.1061/JPEODX.0000085.
26. Meng, G.F.; Wang, Y.; Duan, J.Y.; Xiang, S.M.; Pan, C.H. Efficient Image Dehazing with Boundary Constraint and Contextual Regularization. In Proceedings of the 2013 IEEE International Conference On Computer Vision (ICCV), Sydney, Australia, 1–8 December 2013; IEEE: New York, NY, USA, 2013; pp. 617–624.
27. Wu, Y.N.; Abdel-Aty, M.; Cai, Q.; Lee, J.; Park, J. Developing an algorithm to assess the rear-end collision risk under fog conditions using real-time data. *Transp. Res. Part C-Emerg. Technol.* **2018**, *87*, 11–25. https://doi.org/10.1016/j.trc.2017.12.012.

28. Af Drake, P.O.; Willstrand, O.; Andersson, A.; Biswanger, H. Physical characteristics of splash and spray clouds produced by heavy vehicles (trucks and lorries) driven on wet asphalt. *J. Wind Eng. Ind. Aerodyn.* **2021**, *217*, 104734. https://doi.org/10.1016/j.jweia.2021.104734.
29. American Association of State Highway and Transportation Officials. *Policy on Geometric Design of Highways and Streets*; American Association of State Highway and Transportation Officials: Washington, DC, USA, 2001; Volume 1, p. 158.
30. Wang, B.; Chen, T.Y.; Zhang, C.; Wong, Y.D.; Zhang, H.; Zhou, Y.H. Toward safer highway work zones: An empirical analysis of crash risks using improved safety potential field and machine learning techniques. *Accid. Anal. Prev.* **2024**, *194*, 107361. https://doi.org/10.1016/j.aap.2023.107361.
31. Wolf, M.T.; Burdick, J.W. Artificial potential functions for highway driving with collision avoidance. In Proceedings of the 2008 IEEE International Conference on Robotics and Automation, Pasadena, CA, USA, 19–23 May 2008; pp. 3731–3736.
32. *GB 5768-2009*; Road Traffic Signs and Markings. Standardization Administration of China: Beijing, China, 2009.
33. *GB/T 31444-2015*; Rating of Early-Warning of Road Traffic Under Fog Weather Conditions. National Standards of People's Republic of China: Beijing, China, 2015.
34. Negru, M.; Nedevschi, S. Image based fog detection and visibility estimation for driving assistance systems. In Proceedings of the 2013 IEEE 9th International Conference on Intelligent Computer Communication and Processing (ICCP), Cluj-Napoca, Romania, 5–7 September 2013; pp. 163–168.
35. Singh, D.; Das, P.; Ghosh, I. Surrogate Safety Assessment of Traffic Facilities under Ordered and Disordered Traffic Condition: Systematic Literature Review. *KSCE J. Civ. Eng.* **2023**, *27*, 5008–5029. https://doi.org/10.1007/s12205-023-0979-y.
36. Shi, X.; Wong, Y.D.; Li, M.Z.F.; Chai, C. Key risk indicators for accident assessment conditioned on pre-crash vehicle trajectory. *Accid. Anal. Prev.* **2018**, *117*, 346–356. https://doi.org/10.1016/j.aap.2018.05.007.
37. Wang, C.; Xu, C.C.; Dai, Y.L. A crash prediction method based on bivariate extreme value theory and video-based vehicle trajectory data. *Accid. Anal. Prev.* **2019**, *123*, 365–373. https://doi.org/10.1016/j.aap.2018.12.013.
38. Fu, C.Y.; Sayed, T. Comparison of threshold determination methods for the deceleration rate to avoid a crash (DRAC)-based crash estimation. *Accid. Anal. Prev.* **2021**, *153*, 106051. https://doi.org/10.1016/j.aap.2021.106051.
39. Tawfeek, M.H.; El-Basyouny, K. A perceptual forward collision warning model using naturalistic driving data. *Can. J. Civ. Eng.* **2018**, *45*, 899–907. https://doi.org/10.1139/cjce-2017-0592.
40. Tawfeek, M.H. Human-like speed modeling for autonomous vehicles during car-following at intersections. *Can. J. Civ. Eng.* **2021**, *49*, 255–264. https://doi.org/10.1139/cjce-2020-0761.